A non-local fuzzy segmentation method: Application to brain MRI

Benoît Caldairou [a],*, Nicolas Passat [a], Piotr A. Habas [b], Colin Studholme [b], François Rousseau [a]

[a] LSIIT, UMR 7005 CNRS/Université de Strasbourg, Pôle API, Boulevard Sébastien Brant, BP 10413, 67412 Illkirch CEDEX, France
[b] Biomedical Image Computing Group, Department of Radiology and Biomedical Imaging, University of California San Francisco, 1 Irving Street, San Francisco, CA 94143, USA

ARTICLE INFO

ABSTRACT

The Fuzzy C-Means (FCM) algorithm is a widely used and flexible approach to automated image segmentation, especially in the field of brain tissue segmentation from 3D MRI, where it addresses the problem of partial volume effects. In order to improve its robustness to classical image deterioration, namely noise and bias field artifacts, which arise in the MRI acquisition process, we propose to integrate into the FCM segmentation methodology concepts inspired by the non-local (NL) framework, initially defined and considered in the context of image restoration. The key algorithmic contributions of this article are the definition of an NL data term and an NL regularisation term to efficiently handle intensity inhomogeneities and noise in the data. The resulting new energy formulation is then built into an NL-FCM brain tissue segmentation algorithm. Experiments performed on both synthetic and real MRI data, leading to the classification of brain tissues into grey matter, white matter and cerebrospinal fluid, indicate a significant improvement in performance in the case of higher noise levels, when compared to a range of standard algorithms.

1. Introduction

Magnetic Resonance Imaging (MRI) is one of the most common ways to visualise brain structures. Based on this imaging technique, the study of the main cerebral tissues (namely, white matter (WM) and grey matter (GM)) is a key point in the context of computer-aided diagnosis and patient follow-up. Such a study generally requires to first perform a segmentation step, which aims at partitioning the intra cranial volume into—potentially overlapping—parts: WM, GM, and cerebrospinal fluid (CSF). When dealing with MRI brain data, the principal challenge related to segmentation is generally the correct handling of the following image deterioration elements: (i) acquisition noise, (ii) partial volume effect (PVE) (i.e., the mixture of several tissue signals in a same voxel, induced in particular by the image resolution), and (iii) bias field (i.e., spatial intensity inhomogeneity, physically linked to the radiofrequency MR signal [1]).

A huge literature is devoted to brain segmentation from 3D MRI data. Indeed, segmentation methods can deal with a large spectrum of purposes:

- extraction of one or several specific and/or small structures, e.g., cortex [2,3], sulci [4,5], sub-cortical structures [6,7];
- partition of the brain into main anatomical structures [8–10];

- extraction of the main tissues, i.e., partitioning of the intracranial volume into WM, GM and CSF [11–14].

This last topic is the one considered in this work. The corresponding state of the art methods can be categorised by considering their methodological approach [15]; non-exhaustively, one can distinguish classifiers, Markov random field (MRF), artificial neural networks, and deformable models. In this article we focus on classification-based methods devoted to the segmentation of adult brain tissues into three classes: white matter (WM), grey matter (GM), and cerebrospinal fluid (CSF). We begin with a review of current published approaches to this problem.

Classification methods dealing with brain MRI data can be divided into two groups: parametric and non-parametric. Most of the parametric methods make the assumption that the three brain tissue types present a MR signal which follows a Gaussian distribution. In this case, the statistical model parameters are usually estimated using a maximum likelihood (ML) or maximum a posteriori (MAP) approach and the expectation–maximisation (EM) algorithm is used for the optimisation process. In order to reduce the effects of noise, a regularisation term taking into account local interactions between voxels is commonly added, relying for instance on MRF [16–18] or hidden Markov chains [13]. Alternatively to statistical parametric methods, unsupervised non-parametric schemes have been recently proposed for

* Corresponding author. Tel.: +33 3 68 85 44 13.
 E-mail address: benoit.caldairou@unistra.fr (B. Caldairou).

adult brain MRI segmentation [11,14]. One such approach is the mean-shift algorithm, whose key points include the fact that no initial clusters are required and that the number of distinct tissue clusters is estimated from the data. The assumptions required for parametric approaches to statistical tissue distributions are then avoided.

In order to complete this review of the current state of the art in tissue classification methods, let us now consider Fuzzy C-Means (FCM) based approaches [19,20]. The principle of these clustering techniques is to estimate three clusters by iteratively computing a mean intensity for each class being considered (GM, WM, CSF). A soft segmentation compensating for PVE artifacts is then obtained by computing the distances between the intensity of a voxel and the means of each of the different classes. To decrease the algorithm sensitivity to noise and intensity inhomogeneity, the FCM framework can be easily extended by incorporating information about multiple channels [21], spatial regularisation [22], topological constraints [9], bias field correction [21,23].

In this article, which is an extended version of the conference paper [24], we especially consider the use of a FCM based methodology for brain MRI segmentation. To deal with the three main image degradation elements listed above (namely, noise, PVE and bias field), we investigate the use of a non-local framework which has been recently proposed for denoising purpose [25]. Since then, this non-local strategy has been studied and applied in several image processing applications such as non-local regularisation functionals in the context of inverse problems [26–29]. More generally, the non-local methodology has led to the design of powerful algorithms providing, in particular, an ability to efficiently handle repetitive structures and textures. In this context, the main contributions proposed in this article are:

1. the definition of a non-local image data term in the FCM framework, devoted to deal with intensity inhomogeneity (Section 3.2);
2. the definition of a non-local regularisation term to cope with image noise (Section 3.3);
3. an exhaustive evaluation of the contribution of the non-local methodology to the FCM framework using both synthetic and real MRI data (Section 4).

This article is organised as follows. In Section 2, we present the segmentation problem and provide a short overview of the FCM framework and some extensions to deal with MR image artifacts. Section 3 details how the non-local approach is introduced in the FCM methodology for brain MRI segmentation. In Section 4, results obtained on 3D cerebral data from both Brainweb [30] and the Internet Brain Segmentation Repository (IBSR) are presented.

Finally, Section 5 discusses the contribution of the work and examines future directions for development.

2. Background notions

2.1. Fuzzy C-Means

The Fuzzy C-Means (FCM) algorithm integrates the fuzzy sets approach [19] into the classical K-Means algorithm [31]. The FCM approach is presented in detail in [32,33], but in the context of our work, the FCM approach can be formulated as follows.

Let us consider an image composed of a set of points (voxels) Ω, each point $j \in \Omega$ having a given value (grey-level) y_j. Let us suppose that this image has to be segmented into C (≥ 2) classes, in a fuzzy fashion. This means that a voxel j does not necessarily belong to *one* of the C classes, but can "partially" belong to *several* ones. For each voxel $j \in \Omega$, let $(u_{jk})_{k=1}^{C} = (u_{j1}, u_{j2}, \ldots, u_{jC})$ be the membership ratios of j with respect to these C classes, such that $\sum_{j=1}^{C} u_{jk} = 1$ and $u_{jk} \in [0,1], \forall k \in [\![1,C]\!]$. For each class k, let $\mathbf{v}_k$ be the centroid of this class (which usually corresponds to the mean grey-level value of this class of voxels). Based on these notations, in the FCM approach, the segmentation process of a grey-level image can be defined as the minimisation of an energy function

$$J_{FCM} = \sum_{j \in \Omega} \sum_{k=1}^{C} u_{jk}^q \|\mathbf{y}_j - \mathbf{v}_k\|_2^2 \tag{1}$$

where $\|.\|_2$ is the Euclidean norm. Then, $\|\mathbf{y}_j - \mathbf{v}_k\|_2^2$ is actually the Euclidean squared distance (in the grey-level space) between the value of the voxel j and the centroid of the class k. Note that the parameter q (generally set to 2) enables the control of the fuzziness of the segmentation (in particular, when q gets close to 1, the segmentation tends to converge onto a binary result).

The energy function J_{FCM} can be easily minimised using a gradient-based iterative algorithm which alternatively computes the membership ratios u_{jk} and the centroids $\mathbf{v}_k$ [21]. It has to be noted here that the FCM method generally tends to converge rapidly to a stable solution.

By definition, the FCM approach is intrinsically able to deal efficiently with PVE artifacts, since voxels presenting PVE are simply allowed to belong to several classes by the FCM, as illustrated in Fig. 1. It must be noted here that the image depicted in Fig. 1(a) is of very high quality, being corrupted neither by noise nor by bias field.

In the case of images of lower quality, altered in particular by noise and/or bias field—which is generally the case when considering clinical MRI data—the performance of FCM methods strongly decreases. In the case of noisy images (illustrated in Fig. 2), anatomically erroneous structures may appear (in the form of "salt and pepper" noise in the resulting segmentation), for instance single GM voxels within homogeneous WM. In the case
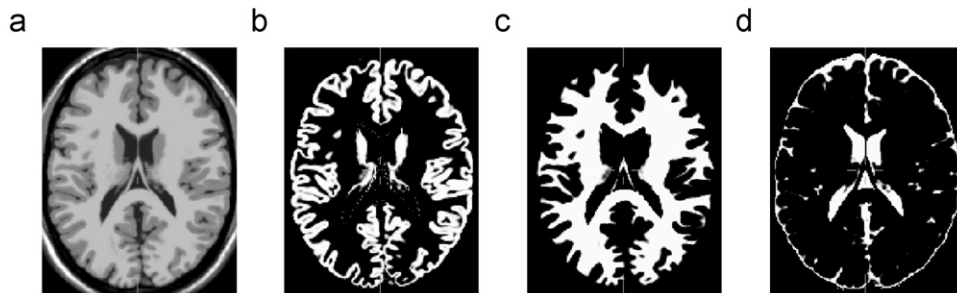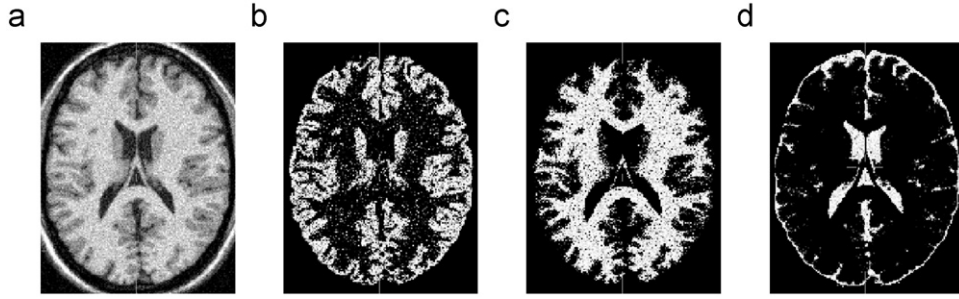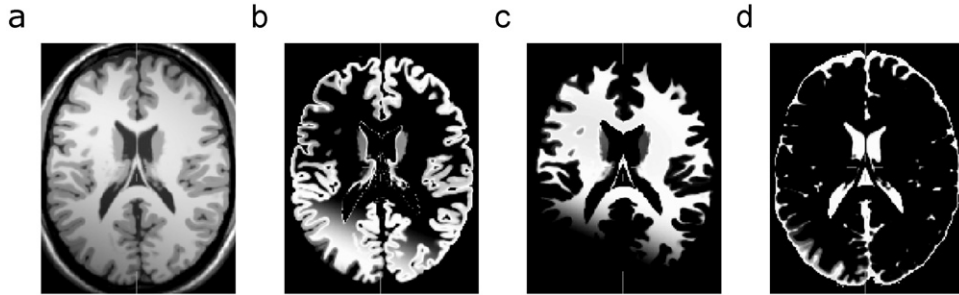

Fig. 1. FCM segmentation in case of partial volume effect. (a) A brain MRI slice. (b–d) Results of the segmentation of (a): (b) GM, (c) WM, (d) CSF.

Fig. 2. FCM segmentation in case of noise. (a) A brain MRI slice (similar to the one of Fig. 1(a)) altered by noise. (b–d) Results of the segmentation of (a): (b) GM, (c) WM, (d) CSF.

Fig. 3. FCM segmentation in case of bias field. (a) A brain MRI slice (similar to the one of Fig. 1(a)) altered by bias field. (b–d) Results of the segmentation of (a): (b) GM, (c) WM, (d) CSF.

of images altered by bias field (illustrated in Fig. 3), significantly sized clusters of voxels may be erroneously classified, possibly leading to significant errors in tissue volume estimates.

Fortunately, in order to deal with these different issues, the FCM methodology can be extended. In particular, several approaches have been proposed to improve its robustness to artifacts, for instance by including bias field correction (Section 2.2) and regularisation (Section 2.3).

2.2. Bias field correction

Since the bias field is a smooth variation of the MR signal within tissues across the image, the correction methods proposed in the literature generally consider it as an additional feature which can be modelled either as a smooth non-parametric gain field using a derivative-based regularisation approach [21], a smooth polynomial surface [23,9] over the image, or a stack of smooth B-Spline surfaces with enforced continuities across slices [34].

When the bias field is modelled as a slowly varying multiplicative field, it can be included into the segmentation energy function to be minimised. This leads to a modified expression of the term J_{FCM} [21], previously defined in Eq. (1)

$$J_{B\text{-}FCM} = \sum_{j \in \Omega} \sum_{k=1}^{C} u_{jk}^q \| \mathbf{y}_j - \mathbf{b}_j . \mathbf{v}_k \|_2^2 \qquad (2)$$

where $\mathbf{b}_j$ is the bias field measured at voxel j. Since such a computational approach may not lead to a smooth estimation of the bias field, the use of this strategy can require an additional regularisation term (parametric [23,34] or non-parametric [21]).

Rather than assuming the presence of a single multiplicative field applied over the image data, an alternative approach is to allow the spatial variation of each tissue class to vary independently across the image, to, for example, allow changes across white matter that do not occur in grey matter. Although not motivated by the most common coil induced MR intensity inhomogeneity, such a formulation can capture other important effects, such as those relating to

the variation of underlying tissue properties, and other scanner related signal inhomogeneities. Following this idea, and using a local image model for brain tissue clustering, an FCM-based algorithm which does not require any explicit bias field correction has been proposed in [35]. This approach is the one which has been followed in our work to tackle the problem of intensity inhomogeneity. Our contribution related to this point (described in Section 3.2) is the use of a non-local approach to estimate locally the centroids of the brain tissue classes.

2.3. Regularisation

Regularisation is a classic approach to solving inverse problems, enabling the determination of the most suitable solution among several possible ones [36]. It has inspired methods relying on Markov random field [16] or on Markov random chains (MRC) [13] which introduce (global or partial) spatial constraints to eliminate non-relevant solutions. In the FCM framework, the regularisation process increases the robustness of the clustering algorithm with respect to the image noise [22,23,37,38].

In particular in [22], a regularisation term is added in Eq. (1), in order to penalise unlikely configurations of labels in the image segmentation. The resulting method is called the Robust Fuzzy C-Means algorithm (R-FCM). The resulting expression for the energy function becomes

$$J_{R\text{-}FCM} = \underbrace{\sum_{j \in \Omega} \sum_{k=1}^{C} u_{jk}^q \| \mathbf{y}_j - \mathbf{v}_k \|_2^2}_{J_{FCM}} + \underbrace{\frac{\beta}{2} \sum_{j \in \Omega} \sum_{k=1}^{C} u_{jk}^q \sum_{n \in N_j^R} \sum_{l \in L_k} u_{nl}^q}_{J_{Reg}} \qquad (3)$$

where N_j^R is the set of the neighbours of voxel j and $L_k = [\![1, C]\!] \setminus \{k\} = \{1, \ldots, k-1, k+1, \ldots, C\}$. The parameter β controls the trade-off between the data term J_{FCM} and the smoothing term J_{Reg}. If $\beta = 0$, the formulation reverts to the classic FCM algorithm without any regularisation term. If $\beta > 0$, the dependency on the neighbours causes u_{jk} to be large when the neighbouring
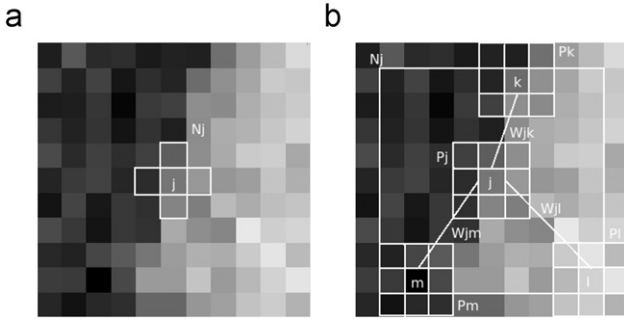
Fig. 4. Comparison of (a) the R-FCM [22] and (b) the NL approaches. In this example, the area around the voxel j is much more similar to the one of voxel k than the ones of voxels m and l. Therefore, the weight w_{jk} will be higher than the weights w_{jm} and w_{jl}.

membership values of the other classes are small. The result is a smoothing effect that causes neighbouring membership values of a class to be negatively correlated with the membership values of other classes. Broadly speaking, minimising this regularisation term is equivalent to encouraging the formation of regions of homogeneous class composition. In [22], the use of cross-validations was proposed as a way to estimate β and obtain near-optimal performance, with a neighbourhood (N_j^R) composed of 6-adjacent neighbours to the given voxel j (see Fig. 4(a) for a 2-D illustration).

In the work proposed here, we focus on an approach for regularisation similar to that of in the R-FCM algorithm, but instead using a larger weighted neighbourhood that can make use of a non-local framework.

3. Non-local framework

3.1. Definition

The non-local (NL) regularisation is a strategy that has been proposed first as a denoising tool [25] and named as NL mean denoising. Essentially, it aims to take advantage of the redundancy present in natural structures; broadly speaking a small neighbourhood around a voxel may match neighbourhoods around other voxels within the same scene.

This framework relies on a weighted graph w that links together voxels over the image domain. The computation of this graph w is based on the similarity between neighbourhoods of voxels (see Fig. 4(b)). In the following formulation we will refer to such a neighbourhood as a *patch*, and denote the patch around voxel j as P_j. The similarity of two voxels i and j is defined as the similarity of the grey-levels contained within P_i and P_j. This similarity can be computed as a Gaussian weighted Euclidean distance [25], but it has been shown that a Euclidean distance is actually reliable enough [39]. The weight w_{ij} for the voxels i and j is defined as

$$w_{ij} = \frac{1}{Z_i} e^{-1/h^2 \|\mathbf{y}(P_i) - \mathbf{y}(P_j)\|_2^2} \tag{4}$$

where the distance between the patches P_i and P_j is

$$\|\mathbf{y}(P_i) - \mathbf{y}(P_j)\|_2^2 = \sum_{p=1}^{|P_i|} (y^{(p)}(P_i) - y^{(p)}(P_j))^2 \tag{5}$$

The term Z_i is a normalisation constant, while h is a smoothing parameter. The vector $\mathbf{y}(P_i)$ contains the grey-level profile in the neighbourhood of the voxel i and $y^{(p)}(P_i)$ is the pth component of this vector.

Note that it is possible to set the parameter h automatically [39] by using $h^2 = 2\alpha\sigma^2 |P_i|$. In this formulation, σ, namely the standard deviation of the noise, can be computed directly from the image. If the noise in the image is Gaussian, the parameter α can be fixed to 1 [39]; otherwise, it can be adjusted to provide a more accurate result.

The use of the NL regularisation approach has already been investigated for different kinds of image processing problems. In [26,29] it has been used to constrain a deconvolution process, while in [28] it has been proposed as a route to providing resolution enhancement during image reconstruction. It has also been used in segmentation by replacing the original Euclidean distance by a measure which includes a balance between local and non-local information [40].

The key point of the NL approach is the ability to handle large neighbourhoods without prior knowledge. We show in this work that this NL methodology can be integrated into the FCM framework. Indeed, we define:

1. a non-local data term J_{NL-FCM} (Section 3.2) which can cope with intensity inhomogeneity;
2. a non-local regularisation term J_{NL-Reg} (Section 3.3) which can deal with image noise.

3.2. Non-local energy function

As stated above, the standard FCM approach assumes that cluster centroids are spatially invariant over the image space. Consequently, the FCM algorithm can be sensitive to intensity inhomogeneity artifacts occurring in MRI data. In order to tackle this problem without relying on *ad hoc* prior knowledge related to this inhomogeneity, it is possible to incorporate a non-local data term into the FCM energy function provided in Eq. (1). This term enables to relax the spatial stationarity assumption related to cluster centroids.

The following data term, designed for this purpose, integrates non-local weights $w_{j\star}$ associated with different patches located in an extended neighbourhood N_j around the voxel of interest j

$$J_{NL\text{-}FCM} = \sum_{j \in \Omega} \sum_{k=1}^{C} \sum_{n \in N_j} w_{jn} u_{jk}^q \|\mathbf{y}_j - \mathbf{v}_{kn}\|_2^2 \tag{6}$$

Compared to the standard data term of Eq. (1), two main differences have to be observed: (i) each cluster centroid is no longer assumed to be spatially invariant and thus presents a specific value ($\mathbf{v}_{kn}$) for each point of the image, and (ii) each point of the extended neighbourhood does not necessarily have the same influence, based on a specific non-local graph w modelling the similarity between image patches. In particular, this graph w penalises the points n which are surrounded by a patch less similar to the patch around the current point j (w_{jn} is low), allowing the points surrounded by the same kind of patches as j to have greater influence.

The local centroid ($\mathbf{v}_{kj}$) is computed for each voxel j over a local neighbourhood denoted M_j (the impact of the size of this neighbourhood is studied in Section 4.2.1).

3.3. Non-local regularisation

In the FCM regularisation context, we investigate the use of neighbourhoods larger than those considered in previous work [22] which can then provide more information to the regularisation process. The underlying assumption is that voxels which have similar patches in the search area belong to the same tissue, as illustrated in Fig. 4(b).

Consequently, we propose to define a NL version for FCM regularisation, with the following formulation

$$J_{NL\text{-}Reg} = \frac{\beta}{2} \sum_{j \in \Omega} \sum_{k=1}^{C} u_{jk}^q \sum_{n \in N_j^R} w_{jn} \sum_{l \in L_k} u_{nl}^q \qquad (7)$$

Compared to Eq. (3), a weight parameter (w_{jn}) is introduced in order to automatically balance the influence of voxels in the neighbourhood N_j^R. Note also that, in contrast to [22], where N_j^R is defined as a six-adjacency neighbourhood, here we explore the use of large scale neighbourhoods, such as the ones used in the non-local denoising approach described in [25].

The regularisation term of the energy function defined in Eq. (7) takes into account the image content to smooth the current segmentation map in an adaptive and flexible manner. Broadly speaking, if the neighbourhoods of two voxels j and n are similar, it is more probable that these voxels belong to the same tissue and so, the weight w_{jn} increases. Conversely, if these two voxels are quite different in the original image, the influence of the regularisation term should be decreased, since there is a lower probability that the voxel n might have a strong influence on the classification of the current voxel j.

3.4. Overview

By combining the non-local data term J_{NL-FCM} and the non-local regularisation term J_{NL-Reg} introduced above, we obtain a fully non-local regularised energy function, which enables us to simultaneously deal with noise and inhomogeneity artifacts within the image data,

$$J_{NL\text{-}R\text{-}FCM} = J_{NL\text{-}FCM} + J_{NL\text{-}Reg}$$

$$= \sum_{j \in \Omega} \sum_{k=1}^{C} \sum_{n \in N_j} w_{jn} u_{jk}^q \|\mathbf{y}_j - \mathbf{v}_{kn}\|_2^2 + \frac{\beta}{2} \sum_{j \in \Omega} \sum_{k=1}^{C} u_{jk}^q \sum_{n \in N_j^R} w_{jn} \sum_{l \in L_k} u_{nl}^q \quad (8)$$

It must be noted that the weights w_{jn} of the J_{NL-Reg} and J_{NL-FCM} may be distinct, since they are actually not used for the same purpose. Similarly, the neighbourhoods N_j and N_j^R may have a different size. For the sake of simplicity, we will, however, consider in this work that, for the same pair (j,n), both w_{jn} weights have the same value, and $N_j = N_j^R$.

The final NL-FCM method using the proposed energy function can be summarised as follows:

1. compute w_{jn} for all $(j,n) \in \Omega^2$;
2. compute $\mathbf{v}_{kn}$ for all $(k,n) \in [\![1,C]\!] \times \Omega$ (initial cluster centroid evaluation);
3. compute u_{jk} for all $(j,k) \in \Omega \times [\![1,C]\!]$ (initial fuzzy clustering);
4. repeat;
   (a) recompute $\mathbf{v}_{kn}$ for all $(k,n) \in [\![1,C]\!] \times \Omega$;
   (b) recompute u_{jk} for all $(j,k) \in \Omega \times [\![1,C]\!]$.
   Until minimising $J_{NL-R-FCM}$.

The inputs of this algorithm are the image data (providing Ω and the $\mathbf{y}$ values) and the number of classes C. The parameters determining its behaviour are the size and shape of the neighbourhoods N_j. β value controls the trade-off between the two terms.

The proposed method (and the other ones further considered for validation, namely FCM and R-FCM) were optimised as proposed in [22]. In particular, the same analytical expressions were used for the calculation of centroids and membership functions.

4. Experiments

4.1. Evaluation framework

Experiments have been carried out on simulated T1-weighted brain MR images provided by the Brainweb database [30] and on real brain images provided by the Internet Brain Segmentation Repository (IBSR) database.

First, considering the Brainweb dataset, three experimental setups have been investigated to exhaustively test the non-local framework introduced into FCM:

1. evaluation of the non-local energy function using images only corrupted by intensity inhomogeneity (Section 4.2.1);
2. evaluation of the non-local regularisation using images only corrupted by Rician noise [41] (Section 4.2.2);
3. evaluation of the non-local FCM framework using images corrupted by both intensity inhomogeneity and Rician noise (Section 4.2.3).

Second, the proposed non-local FCM algorithm has been applied on IBSR brain images. In both cases, a ground truth is used to quantify the quality of the segmentation results and the Kappa Index (KI) overlap measure is used

$$KI = \frac{2 \cdot TP}{2 \cdot TP + FP + FN} \qquad (9)$$

where TP is the number of true positives, FP is the number of false positives and FN, the number of false negatives.

4.2. Results on Brainweb images

BrainWeb[1] is a database, providing (among others) simulated brain MRI data for several acquisition modalities (T1, T2, etc.) and acquisition parameters. Each 3-D image is provided with anatomical ground truth which provides tissue class label for each intracranial voxel. For the proposed experiments, the considered BrainWeb data have been chosen with classical acquisition parameters (with respect to a standard brain MRI acquisition), namely by considering T1-weighting, with 1 mm resolution, leading to a size of $181 \times 217 \times 181$ voxels. The repetition time is equal to 18 ms and the echo time has been set to 10 ms.
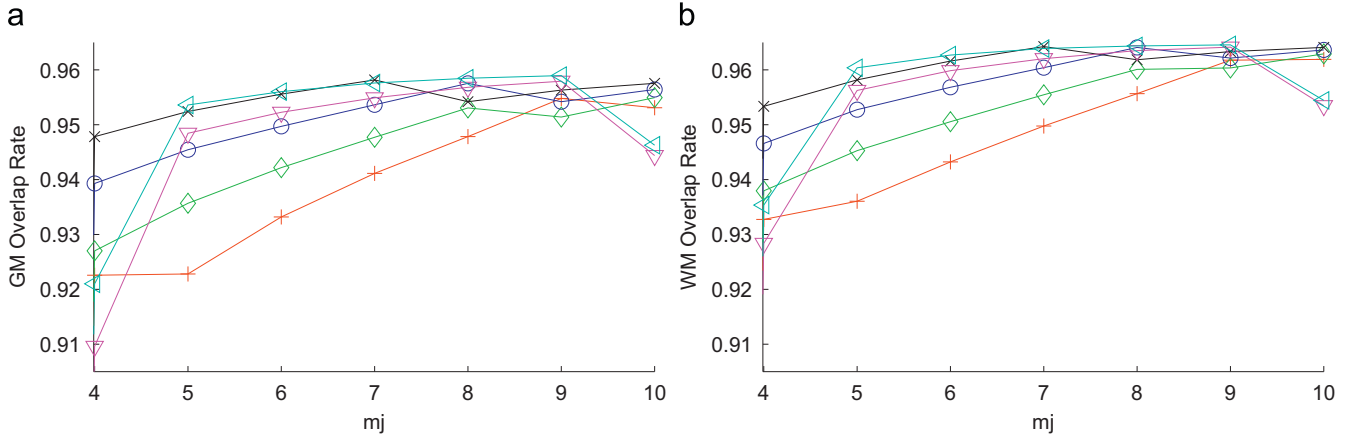
4.2.1. Study of the non-local energy function

Experiments were carried out to determine the influence of the size of the neighbourhoods M_j and N_j used in the non-local energy function. M_j is the size of the neighbourhood used in the computation of the local centroids $\mathbf{v}_{kl}$, and we define m_j as: $|M_j| = (2 \cdot m_j + 1)^3$, $m_j \in [\![4,10]\!]$. N_j is the size of the neighbourhood used for the computation of the non-local weights $w_{j\star}$, and n_j is then defined as: $|N_j| = (2 \cdot n_j + 1)^3$, $n_j \in [\![4,10]\!]$. (The interval bounds for m_j and n_j have been experimentally set to 4 and 10 to find a satisfying compromise between computation time and performances.)

Fig. 5 shows the evolution of the mean overlap measures for the classes WM and GM depending on the values of n_j and m_j. Based on these results, we chose a couple that was small enough for not slowing the computation down while providing good performance: $(n_j, m_j) = (8,8)$.

The proposed non-local energy function was compared with the FCM function [33]. Fig. 6 shows the segmentation results and the resulting overlap measures are reported in Table 1. As shown in Section 2, the FCM algorithm is not adapted to intensity

---

[1] http://www.bic.mni.mcgill.ca/brainweb/

Fig. 5. Influence of parameters N_j and M_j in the non-local energy function on the mean overlap values computed for (a) grey matter and (b) white matter. Legend : $(+)$ $n_j=4$, $(\diamond)$ $n_j=5$, $(\circ)$ $n_j=6$, $(\times)$ $n_j=7$, $(\triangledown)$, $n_j=8$, $(\triangleleft)$, $n_j=9$.
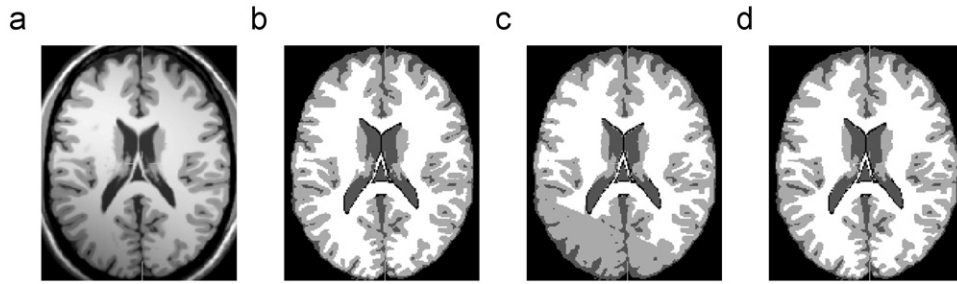
Fig. 6. Segmentation results of the Brainweb T1-weighted image only corrupted by intensity inhomogeneity. (a) Original image, (b) Brainweb segmentation ground truth, (c) FCM segmentation, (d) NL-FCM segmentation ($m_j=8$ and $n_j=8$).

Table 1
Mean overlap measures for the WM/GM/CSF segmentation of the Brainweb image corrupted by intensity inhomogeneity ($m_j=8$ and $n_j=8$).

Methods	CSF	GM	WM
FCM [33]	73.84	69.15	75.83
NL-FCM	96.65	95.68	96.35

Three different bias fields have used to corrupt the Brainweb image.

inhomogeneity since the class centroids are assumed to be stationary over the entire image.

Conversely, the proposed non-local framework greatly improves the WM/GM/CSF segmentation even though no explicit evaluation of the bias-field is performed.

4.2.2. Study of the non-local regularisation

The key parameters of the regularisation framework are α and N_j^R. α is a smoothing parameter (related to the parameter h, Eq. (4)) involved in the computation of the non-local graph w and N_j^R is the cubic neighbourhood used in the regularisation term (see Eq. (7)). We define n_j^r such that $|N_j^R| = (2 \cdot n_j^r + 1)^3$. The results for different values of n_j^r ($n_j^r \in [\![1,6]\!]$) are stated in Fig. 7(a). These experiments emphasise that considering extended neighbourhoods is a way to improve the segmentation results. However, increasing n_j^r above 2 does not significantly refine the segmentation results and slows the computation down. We therefore chose to run the validations described below with $n_j^r=2$ (i.e., with $5 \times 5 \times 5$ cubic neighbourhoods).

We have also investigated the influence of the smoothing parameter α (defined in Section 3.1) on the segmentation results. Fig. 7(b) shows that, in agreement with Buades et al. [25], values

of α around 1 provide the best results. Moreover, it can be observed that the algorithm is not sensitive to this parameter if its value is set above 1 (α is set to 1.1 for the validations in the following experiments).

To evaluate the contribution of the non-local framework to the efficiency of the segmentation process, we have also compared the following versions of FCM:

1. FCM [33];
2. R-FCM [22];
3. R-FCM with adaptive non-local weights, i.e., N_j^R is defined as being the 6-adjacency neighbourhood in Eq. (7);
4. NL-Reg with fixed weights, i.e., the w_{jn} weights are set to 1 in Eq. (7);
5. NL-Reg with adaptive non-local weights, i.e., Eq. (7) is applied in its most general form.

The resulting segmentation overlap measures are reported in Table 2. The non-local regularisation approach improves the segmentation results with respect to FCM and R-FCM. The comparison between R-FCM and NL-Reg without weights shows that using a larger neighbourhood leads to significant improvements especially for GM and WM (approx. 1%). Moreover, for the extended neighbourhood, introducing the NL approach results in an improved overlap measure.

Fig. 8 provides an illustration of these improvements, particularly with regard to the GM and CSF performance. The observed differences may be due to the low contrast between CSF and GM in a noisy image which can, however, be correctly handled by the NL regularisation framework. In addition, we observed that the NL-Reg results resolve fine structure more clearly, as seen in the borders between ventricles and GM, and
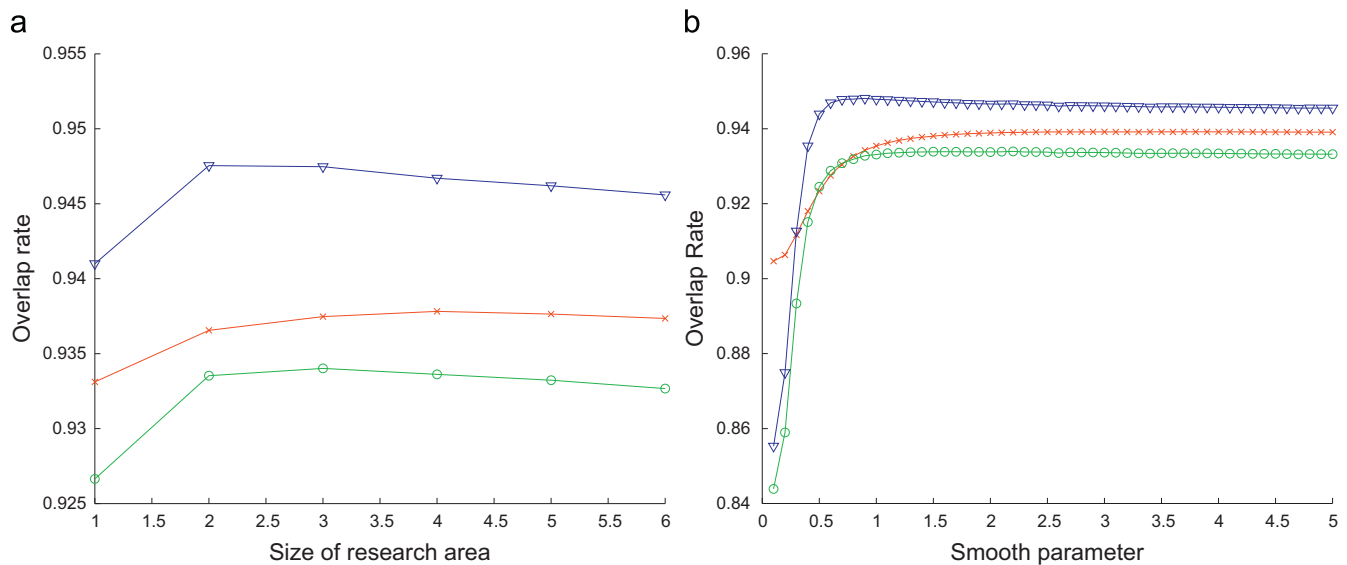
Fig. 7. Influence of NL regularisation parameters. Application on the Brainweb T1-weighted image with 9% Rician noise. (a) Overlap rate w.r.t. the value of n_j^r and (b) overlap rate w.r.t. the smoothing parameter α. Legend: GM ($\circ$), WM ($\triangledown$), CSF ($\times$).

Table 2
Application of different segmentations on a Brainweb T1-weighted image with a 9% Rician noise.

Methods	CSF	GM	WM
FCM [21]	90.46	84.36	85.48
R-FCM [22]	92.09	91.12	92.91
R-FCM (adaptive weights)	92.76	91.09	92.49
NL-Reg	92.22	92.22	94.12
NL-Reg (adaptive weights)	93.63	93.35	94.77

Comparison of the different overlap rates for CSF, GM and WM.

around cortical sulci as depicted by the enlarged views of the R-FCM segmentation in Fig. 8(h) and of the NL-Reg segmentation in Fig. 8(i), when compared to the ground truth in Fig. 8(g).

We carried out complementary experiments to determine the robustness to noise for FCM [33], R-FCM [22] and NL-Reg with Brainweb T1-weighted images with varying noise levels (see Fig. 9). It can be seen that NL-Reg begins to emerge as a strong approach at noise level of 3% and above, and becomes more accurate compared to R-FCM approach at a 5% noise.

4.2.3. Complete algorithm (bias+noise correction)

Experiments are carried out on Brainweb Images corrupted not only by noise, but also by intensity inhomogeneity. To point out the contribution of the regularisation term, we compared the complete algorithm NL-R-FCM to NL-FCM and NL-Reg to an image with a 9% Rician noise and 20% inhomogeneity. The considered parameters are the ones chosen according to the previous experiments, namely $m_j = 8$, $n_j = 8$, and $N_j^R = 5 \times 5 \times 5$. Results are presented in Table 3 and a visual insight of the results is given in Fig. 10.

As expected, including either non-stationary centroids or non-local regularisation enables to significantly improve the segmentation map by comparison to the standard FCM method. Moreover, the simultaneous use of both non-local strategies (NL-R-FCM) leads to complementary segmentation improvements and finally provides the best results.

We carried out supplementary experiments to determine the robustness to noise for the non-local FCM methods with Brainweb T1-weighted images (see Fig. 11). The considered Rician noise

level range is [0,9]%. It appears that the benefits of the NL-R-FCM emerges at 7% noise and above, and especially by comparison to the NL-FCM.

From a computational point of view, each iteration of the algorithm (i.e., computation of the non-local weights, local tissue mean values and the fuzzy classification) requires approximately 1 h, while the algorithm performs generally three or four iterations. This cost is mostly due to the computation of the non-local weights in the data-term, since for each iteration we explore not only a large neighbourhood of each voxel of the image ($|N_j| = 17 \times 17 \times 17$), but also a patch for each voxel of this neighbourhood. The computation time of the non-local regularisation term at each iteration is approximately 1 min, which is explained by the use of a restricted neighbourhood ($|N_j^R| = 5 \times 5 \times 5$) when compared to the one used in the non-local data-term.

4.3. Results on IBSR images

The non-local FCM algorithms were applied to real brain MR datasets (obtained from the Internet Brain Segmentation Repository (IBSR)[2]. This database is a set of 18 3-D images provided with their ground truth segmentation. These images have a size of 256 $\times$ 256 $\times$ 128 voxels, and their resolution vary from 0.8 $\times$ 0.8 $\times$ 1.5 to 1.0 $\times$ 1.0 $\times$ 1.5 mm. (Note that the computation time of an IBSR image is then globally similar to the one of a Brainweb image.)

Since IBSR is a commonly used MRI database for brain tissue segmentation assessment, the obtained results can be directly compared to those provided by the other state of the art methods which also considered IBSR for validations, and in particular the following ones: statistical parametric mapping (SPM 5) [42], expectation-maximisation segmentation (EMS) [16] and hidden Markov chains (HMC) [13].

Based on these considerations, overlap measures were computed for GM and WM and the average results obtained on the 18 cases were compared to the ones of these other methods. Notice that as the expert segmentations of IBSR include only internal CSF

---

[2] These MR brain data sets and their manual segmentations were provided by the Center for Morphometric Analysis at Massachusetts General Hospital and are available at http://www.cma.mgh.harvard.edu/ibsr/.
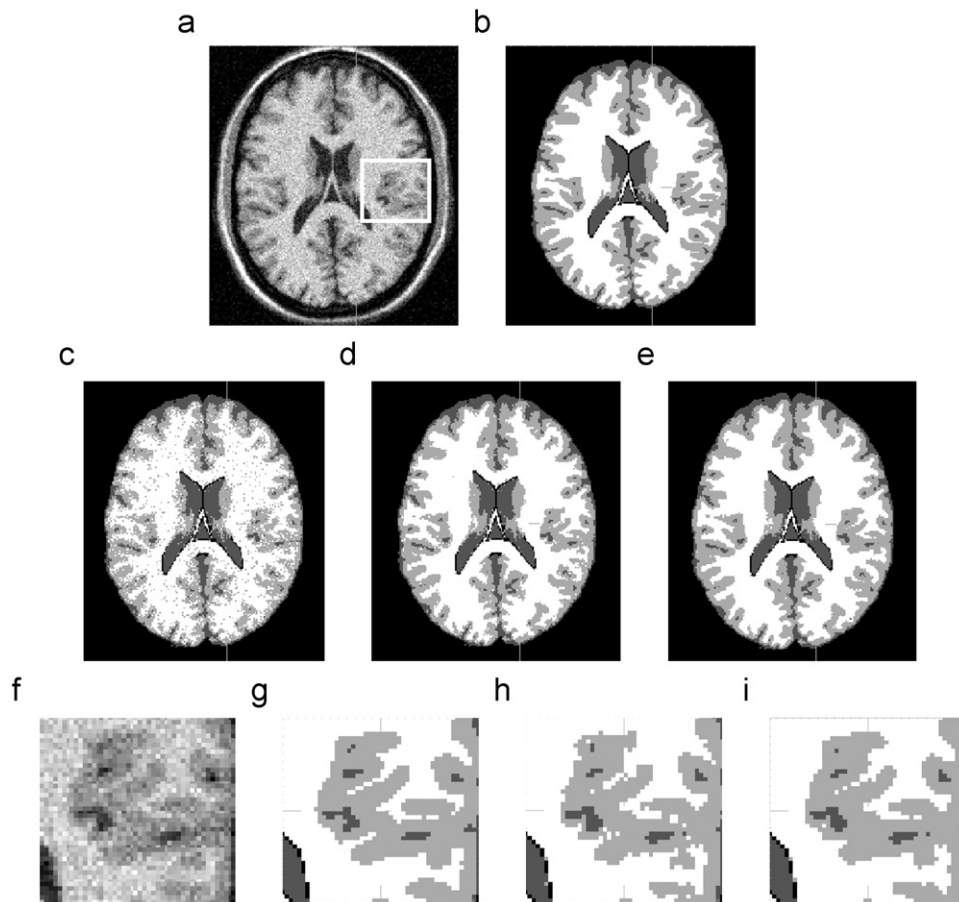
Fig. 8. Results of segmentations on the T1-weighted Brainweb image with a 9% Rician noise. (a) Original image with zoom area, (b) Brainweb segmentation ground truth, (c) FCM segmentation [33], (d) R-FCM segmentation [22], (e) NL-Reg segmentation, (f) zoom on the T1-weighted Brainweb image with a 9% Rician noise, (g) zoom on Brainweb segmentation ground truth, (h) zoom on R-FCM segmentation, (i) zoom on NL-Reg segmentation.
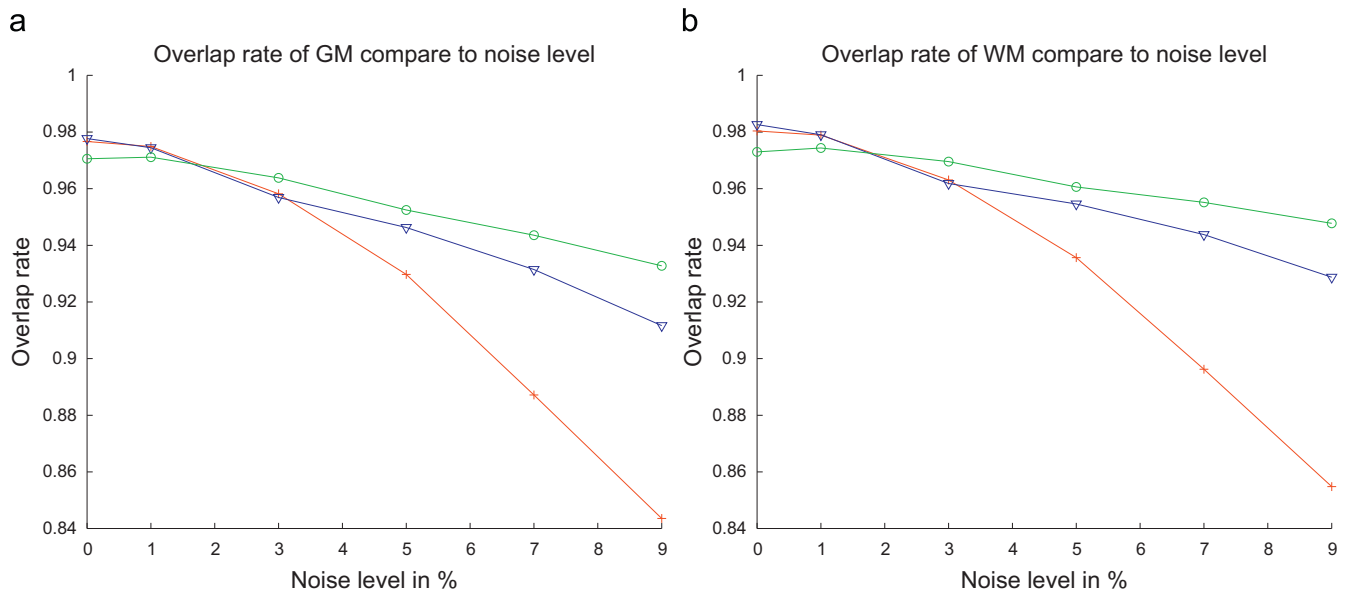
Fig. 9. Application of different techniques on the same Brainweb T1-weighted image with different Rician noise levels. (a) Overlap rate of GM, (b) overlap rate of WM. Legend: NL-Reg (○), R-FCM (▽) [22], FCM (+) [33].

spaces (i.e., the ventricles) while our method also delineates sulcal CSF, we do not report results for cerebrospinal fluid. Quantitative mean results are reported in Table 4 while results for each subject are depicted in Fig. 12.

From the measures of Table 4, it appears that all the segmentation methods considered in these experiments quantitatively provide similar results for the WM. When considering the GM segmentation results, the use of FCM-based

strategies globally leads to better results than the other state of the art methods (both in terms of mean value and standard deviation).

Table 3
Application of different segmentations on a Brainweb T1-weighted image with a 9% Rician noise and 20% intensity inhomogeneity.

| Methods	CSF	GM	WM
FCM [21]	67.45	62.09	69.98
NL-Reg	69.60	64.25	72.16
NL-FCM	84.75	78.1	82.41
NL-R-FCM	87.28	83.52	86.98

Comparison of the different overlap rates for CSF, GM and WM.

From the case results of Fig. 12, it can be observed that the FCM-based methods tend to provide globally similar results. In the few cases where we can distinguish non-homogeneous results (for instance case 4), the best results are obtained without considering non-stationary centroids. A possible cause of this fact may be the global intensity homogeneity of the IBSR data, which do not actually require to correct a potential bias field (see Fig. 13(a)). In this context, the methods that intend to correct such a bias field (namely NL-FCM and NL-R-FCM) may possibly behave in a non-optimal way.

These quantitative results must be interpreted with care, since the ground truth segmentations are not themselves a gold standard but created by an imperfect segmentation process, and thus have limited accuracy in some areas. In particular, for example, on the boundary between CSF and cortical grey matter (Fig. 13(b)), where CSF has been incorrectly replaced by grey
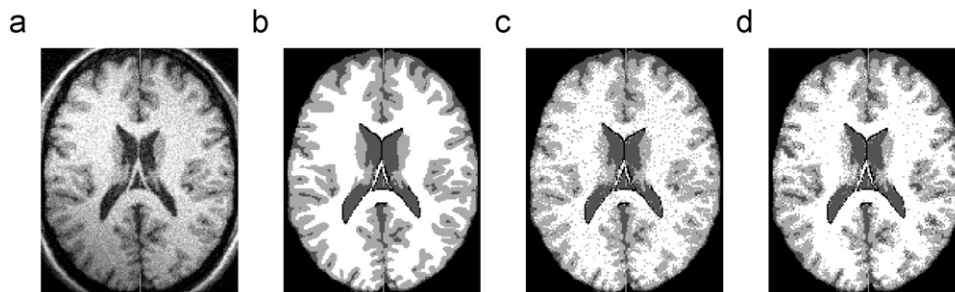
Fig. 10. Segmentation results of the Brainweb T1-weighted image only corrupted by intensity inhomogeneity and a 9% Rician noise. (a) Original image, (b) Brainweb segmentation ground truth, (c) NL-FCM segmentation, (d) NL-R-FCM segmentation ($m_j = 8$ and $n_j = 8$).
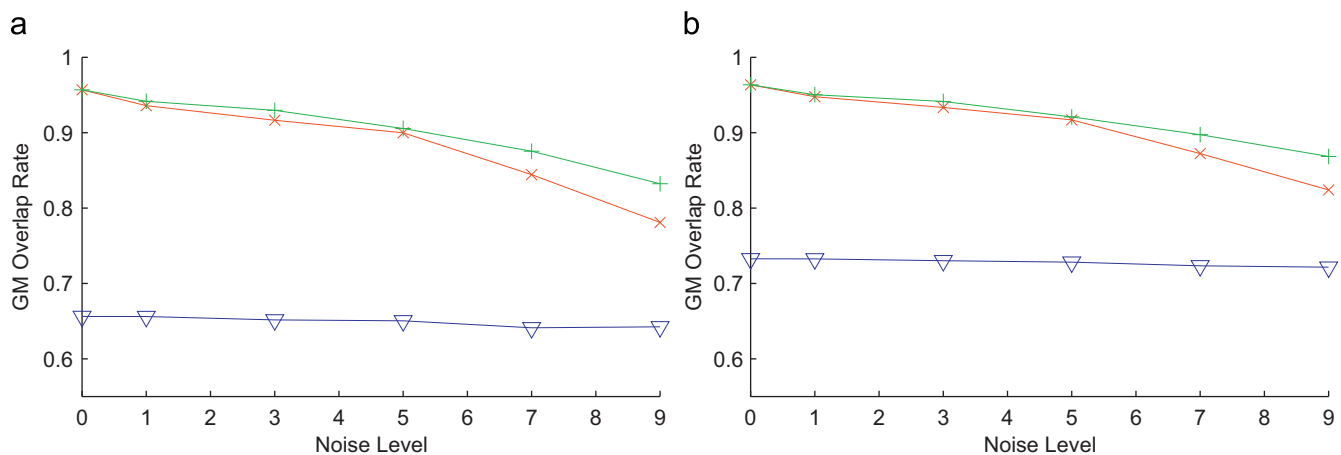

Fig. 11. Application of different techniques on the same Brainweb T1-weighted image with different Rician noise levels and a 20% inhomogeneity. (a) Overlap rate of GM, (b) overlap rate of WM. Legend: NL-Reg ($\triangledown$), NL-FCM ($\times$), NL-R-FCM ($+$).

Table 4
Overlap measures (GM, WM) obtained for different segmentation methods applied on the IBSR database (overlap rates of SPM5, EMS and HMC are from [13]).

Methods	White matter (%)		Grey matter (%)	
	Mean	Standard deviation	Mean	Standard deviation
SPM 5 [42]	85.27	5.52	78.70	13.98
EMS [16]	85.87	2.27	78.94	5.68
HMC [13]	86.53	1.73	79.94	5.57
FCM [21]	85.60	3.81	83.21	4.03
R-FCM [22]	86.09	2.75	84.08	3.98
NL-Reg	86.31	3.18	83.18	4.08
NL-FCM	84.68	3.38	78.84	4.07
NL-R-FCM	84.35	3.38	83.22	3.47
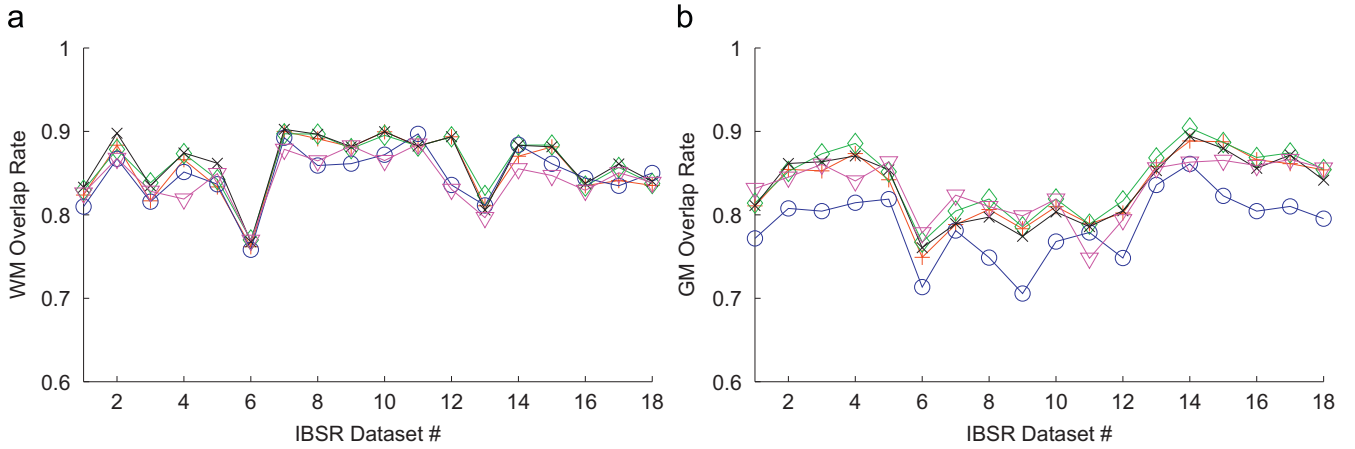
Fig. 12. Application of different segmentation methods through IBSR database. (a) Overlap rate of white matter, (b) overlap rate of grey matter. Legend: FCM (+), R-FCM (◇), NL-Reg (×), NL-FCM (○), NL-R-FCM (▽).
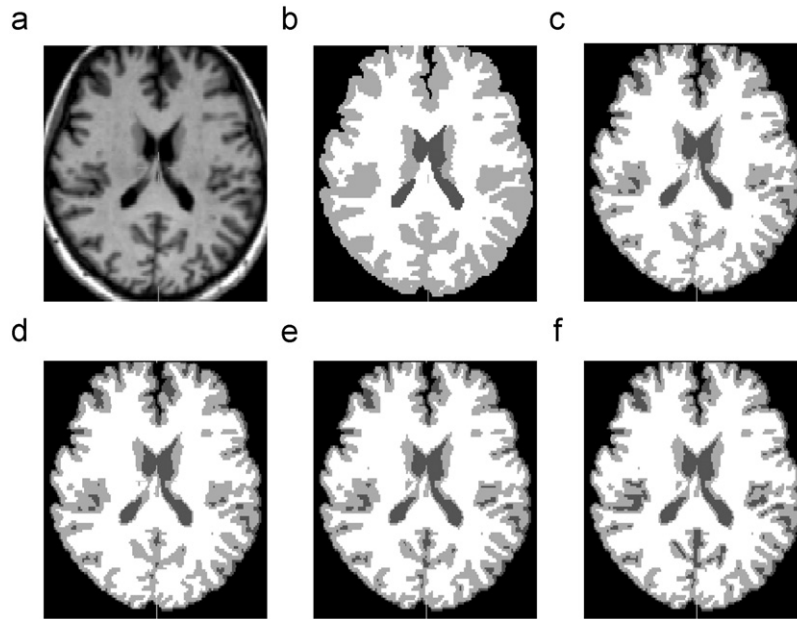
Fig. 13. FCM algorithms applied to IBSR database. (a) A brain MRI slice of case 11 of IBSR Database. (b) Ground truth. (c–f) Results of the segmentation of (a): (c) RFCM, (d) NL-Reg, (e) NL-FCM, (f) NL-R-FCM.

matter. These local errors tend to limit the fidelity of the validation experiments with this data, and quantitative evaluation must be assisted by visual inspection.

To illustrate this point, let us consider the case of the segmentation results shown in Fig. 13 which corresponds to the IBSR image # 11. In Fig. 12, it can be observed that the overlap measure for the GM of the FCM-based method is below 0.8. This low performance is visually justified by comparing the segmentation maps with the provided ground truth obtained by manual delineation. In this manual segmentation, the GM clearly appeared to be oversegmented and then constitutes a superset of the actual GM.

5. Conclusion

In this article, we proposed an extended FCM-based method to unsupervised segmentation, by introducing a non-local formulation for the regularisation and the data-driven terms. By considering data-driven adaptive neighbourhoods, the use of a non-local framework enables to deal with frequent image corruption such as noise and intensity inhomogeneity which are generally observed in MR data. In order to assess the relevance of this non-local FCM approach, it has thus been applied to brain tissue MR segmentation using simulated and real images.

First experiments performed on several noisy (up to 9% Rician noise) and biased (up to 20% inhomogeneity) Brainweb MR images highlight the usefulness of these non-local extensions by efficiently dealing with intensity inhomogeneity and noise. More specifically, it has been experimentally shown that the two non-local functionals (energy function and regularisation) improve the results in a complementary way. Moreover, the resulting method also does not appear to be highly sensitive to parameter settings. Additional experiments, run on real brain MR images from the IBSR database, have shown that this new non-local FCM-based algorithm reliably extracts brain tissue maps with accuracy comparable to state of the art methods (SPM5, EMS, HMC).

From a methodological point of view, further works could now focus on non-local characteristics [43] such as: data-driven estimation of parameters such as (M_j, N_j) and patch sizes, non-local multipoint modelling versus non-local pointwise modelling,

anisotropic patch support, patch parameter dimension reduction, etc. In terms of application, this new approach could be useful in the case of lower contrast imaging (limited by the imaging time, or challenged by inherently low contrast tissue boundaries) for example in the study of the developing human foetus [44].

Acknowledgements

References

[1] J.G. Sled, G.B. Pike, Understanding intensity non-uniformity in MRI, in: Medical Image Computing and Computer-Assisted Intervention—MICCAI'98, Lecture Notes in Computer Science, vol. 1496, Springer, 1998, pp. 614–622.

[2] J.-F. Mangin, V. Frouin, I. Bloch, J. Régis, J. López-Krahe, From 3D magnetic resonance images to structural representations of the cortex topography using topology preserving deformations, Journal of Mathematical Imaging and Vision 5 (4) (1995) 297–318.

[3] R. Goldenberg, R. Kimmel, E. Rivlin, M. Rudzsky, Cortex segmentation: a fast variational geometric approach, IEEE Transactions on Medical Imaging 21 (2) (2002) 1544–1551.

[4] G. Le Goualher, E. Procyk, D.L. Collins, R. Venugopal, C. Barillot, A.C. Evans, Automated extraction and variability analysis of sulcal neuroanatomy, IEEE Transactions on Medical Imaging 18 (3) (1999) 206–217.

[5] F. Yang, F. Kruggel, Automatic segmentation of human brain sulci, Medical Image Analysis 12 (4) (2008) 442–451.

[6] F. Poupon, J.-F. Mangin, D. Hasboun, C. Poupon, I.E. Magnin, V. Frouin, Multi-object deformable templates dedicated to the segmentation of brain deep structures, in: Medical Image Computing and Computer-Assisted Intervention—MICCAI'98, Lecture Notes in Computer Science, vol. 1496, Springer, 1998, pp. 1134–1143.

[7] B. Scherrer, F. Forbes, C. Garbay, M. Dojat, Distributed local MRF models for tissue and structure brain segmentation, IEEE Transactions on Medical Imaging 28 (8) (2009) 1278–1295.

[8] P. Dokládal, I. Bloch, M. Couprie, D. Ruijters, R. Urtasun, L. Garnero, Topologically controlled segmentation of 3D magnetic resonance images of the head by using morphological operators, Pattern Recognition 36 (10) (2003) 2463–2478.

[9] P.-L. Bazin, D.L. Pham, Topology-preserving tissue classification of magnetic resonance brain images, IEEE Transactions on Medical Imaging 26 (4) (2007) 487–496.

[10] C. Ciofolo, C. Barillot, Atlas-based segmentation of 3D cerebral structures with competitive level sets and fuzzy control, Medical Image Analysis 13 (3) (2009) 456–470.

[11] J.R. Jimenez-Alaniz, V. Medina-Banuelos, O. Yanez-Suarez, Data-driven brain MRI segmentation supported on edge confidence and a priori tissue information, IEEE Transactions on Medical Imaging 25 (1) (2006) 74–83.

[12] A. Ferreira da Silva, A Dirichlet process mixture model for brain MRI tissue classification, Medical Image Analysis 11 (2) (2007) 169–182.

[13] S. Bricq, C. Collet, J.-P. Armspach, Unifying framework for multimodal brain MRI segmentation based on Hidden Markov Chains, Medical Image Analysis 12 (6) (2008) 639–652.

[14] A. Mayer, H. Greenspan, An adaptive mean-shift framework for MRI brain segmentation, IEEE Transactions on Medical Imaging 28 (8) (2009) 1238–1250.

[15] D. Pham, C. Xu, J. Prince, Current methods in medical image segmentation, Annual Review of Biomedical Engineering 2 (2000) 315–337.

[16] K. Van Leemput, F. Maes, D. Vandermeulen, P. Suetens, Automated model-based tissue classification of MR images of the brain, IEEE Transactions on Medical Imaging 18 (10) (1999) 897–908.

[17] Y. Zhang, M. Brady, S. Smith, Segmentation of brain MR images through a hidden Markov random field model and the expectation–maximization algorithm, IEEE Transactions on Medical Imaging 20 (1) (2001) 45–57.

[18] Z. Liang, S. Wang, An EM approach to MAP solution of segmenting tissue mixtures: a numerical analysis, IEEE Transactions on Medical Imaging 28 (2) (2009) 297–310.

[19] L.A. Zadeh, Fuzzy sets, Information and Control 8 (3) (1965) 338–353.

[20] D. Pham, J. Prince, X. Chenyang, A. Dagher, An automated technique for statistical characterization of brain tissues in magnetic resonance imaging, International Journal of Pattern Recognition and Artificial Intelligence 11 (8) (1997) 1189–1211.

[21] D.L. Pham, J.L. Prince, Adaptive fuzzy segmentation of magnetic resonance images, IEEE Transactions on Medical Imaging 18 (9) (1999) 737–752.

[22] D.L. Pham, Spatial models for fuzzy clustering, Computer Vision and Image Understanding 84 (2) (2001) 285–297.

[23] M.N. Ahmed, S.M. Yamany, N. Mohamed, A.A. Farag, T. Moriarty, A modified Fuzzy C-Means algorithm for bias field estimation and segmentation of MRI data, IEEE Transactions on Medical Imaging 21 (3) (2002) 993–999.

[24] B. Caldairou, F. Rousseau, N. Passat, P. Habas, C. Studholme, C. Heinrich, A non-local fuzzy segmentation method: application to brain MRI, in: Computer Analysis of Images and Patterns—CAIP'09, Lecture Notes in Computer Science, vol. 5702, Springer, 2009, pp. 606–613.

[25] A. Buades, B. Coll, J.M. Morel, A review of image denoising algorithms with a new one, Multiscale Modeling & Simulation 4 (2) (2005) 490–530.

[26] S. Kinderman, S. Osher, P.W. Jones, Deblurring and denoising of images by nonlocal functionals, Multiscale Modeling & Simulation 4 (4) (2005) 1091–1115.

[27] G. Gilboa, S. Osher, Nonlocal operators with applications to image processing, Technical Report, UCLA CAM, 2007.

[28] F. Rousseau and The Alzheimer's Disease Neuroimaging Initiative, A non-local approach for image super-resolution using intermodality priors, Medical Image Analysis 14 (4) (2010) 594–605.

[29] M. Mignotte, A non-local regularization strategy for image deconvolution, Pattern Recognition Letters 29 (16) (2008) 2206–2212.

[30] C. Cocosco, V. Kollokian, R.-S. Kwan, A. Evans, BrainWeb: online interface to a 3D MRI simulated brain database, in: HBM'97, Proceedings of NeuroImage, vol. 5 (4 Pt 2), 1997, p. S425.

[31] J. MacQueen, Some methods for classification and analysis of multivariate observations, in: Proceedings of Fifth Berkeley Symposium Mathematical Statistics and Probability, Berkeley, California, 1965/66, 1967, pp. 281–297.

[32] J. Bezdek, FCM: the Fuzzy C-means clustering algorithm, Computers and Geosciences 10 (5) (1984) 191–203.

[33] D.L. Pham, J.L. Prince, A.P. Dagher, C. Xu, An automated technique for statistical characterization of brain tissues in magnetic resonance imaging, International Journal of Pattern Recognition and Artificial Intelligence 11 (8) (1996) 1189–1211.

[34] A.W.-C. Liew, H. Yan, An adaptive spatial fuzzy clustering algorithm for 3-D MR image segmentation, IEEE Transactions on Medical Imaging 22 (9) (2003) 1063–1075.

[35] C. Zhu, T. Jiang, Multicontext fuzzy clustering for separation of brain tissues in magnetic resonance images, NeuroImage 18 (3) (2003) 685–696.

[36] A.N. Tikhonov, Regularization of incorrectly posed problems, Soviet Mathematics Doklady 4 (6) (1963) 1624–1627.

[37] W. Cai, S.-C. Chen, D.-Q. Zhang, Fast and robust fuzzy C-means clustering algorithms incorporating local information for image segmentation, Pattern Recognition 40 (3) (2007) 825–838.

[38] Z.M. Wang, Y.C. Soh, Q. Song, K. Sim, Adaptive spatial information-theoretic clustering for image segmentation, Pattern Recognition 42 (9) (2009) 2029–2044.

[39] P. Coupé, P. Yger, S. Prima, P. Hellier, C. Kervrann, C. Barillot, An optimized blockwise nonlocal means denoising filter for 3-D magnetic resonance images, IEEE Transactions on Medical Imaging 27 (4) (2008) 425–441.

[40] J. Wang, J. Kong, Y. Lu, M. Qi, B. Zhang, A modified FCM algorithm for MRI brain image segmentation using both local and non-local spatial constraints, Computerized Medical Imaging and Graphics 32 (8) (2008) 685–698.

[41] R.-S. Kwan, A. Evans, G. Pike, MRI simulation-based evaluation of image-processing and classification methods, IEEE Transactions on Medical Imaging 18 (11) (1999) 1085–1097.

[42] J. Ashburner, K. Friston, Unified segmentation, NeuroImage 26 (3) (2005) 839–851.

[43] V. Katkovnik, A. Foi, K. Egiazarian, J. Ahstola, From local kernel to nonlocal multiple-model image denoising, International Journal of Computer Vision 86 (1) (2010) 1–32.

[44] P.A. Habas, K. Kim, O.A. Glenn, A.J. Barkovich, C. Studholme, A spatio-temporal atlas of the human fetal brain with application to tissue segmentation, in: Medical Image Computing and Computer-Assisted Intervention—MICCAI 2009, Lecture Notes in Computer Science, vol. 5761/2009, Springer, 2009, pp. 289–296.

Benoît Caldairou was born in 1985. He studied Computer Science at CPE Lyon, Lyon, France (M.Sc. 2008) and specialised in image analysis at the Université de St-Etienne, St-Etienne, France (M.Sc. 2008). He is currently pursuing the Ph.D. degree in Computer Science at the University of Strasbourg, Strasbourg, France.

Nicolas Passat was born in 1978. He studied Computer Science at the Université d'Orléans and the Université Strasbourg 1 (M.Sc., 2002; Ph.D., 2005), specialising in image analysis. In 2006, he worked at the A²SI Laboratory (Université de Marne-la-Vallée), as a post-doctoral fellow. Since September 2006, he has been Assistant Professor of Computer Science at the Université de Strasbourg. His scientific interests include mathematical morphology, discrete topology, image segmentation and medical imaging.

Piotr A. Habas received the M.S. degree in Mechatronics from Warsaw University of Technology, Poland in 2002 and the Ph.D. degree in Computer Science and Engineering from University of Louisville, KY in 2007. Since then he has been a member of the Biomedical Image Computing Group at University of California San Francisco, CA. His research interests include medical image analysis and computer-aided diagnosis.

Colin Studholme completed a Ph.D. at the University of London in 1997. His postdoctoral work was carried out at Yale University and he has been faculty at the UCSF since 2000 where he is Associate Professor of Radiology and Biomedical Imaging and leads the Biomedical Image Computing Group.

François Rousseau was born in 1978. He received the Ph.D. degree in signal processing and telecommunications from University of Rennes 1, in 2003. In 2004–2005, he worked at the University of California San Francisco as a post-doctoral fellow. Since 2006, he has been a CNRS research scientist at the LSIIT (Laboratoire des Sciences de l'Image, de l'Informatique et de la Télédétection), Strasbourg.